remote sensing

MDPI

Technical Note

Occurrence Characteristics of Nighttime Merged EIA Based on NASA GOLD Observations from 2018 to 2023

Kun Wu * and Liying Qian

High Altitude Observatory, NSF National Center for Atmospheric Research, Boulder, CO 80301, USA; lqian@ucar.edu

* Correspondence: kunwu@ucar.edu

Abstract: The ionosphere equatorial ionization anomaly (EIA) is usually characterized by two plasma density maxima in the Earth's equatorial region. Merged EIA (MEIA) is a unique phenomenon in the evolution of the EIA. Currently, the occurrence characteristics of MEIA are still not well understood. In this study, we investigate the occurrence characteristics of nighttime MEIA using NASA Global-scale Observations of the Limb and Disk (GOLD) observations between October 2018 and the end of 2023. We found that the occurrence of nighttime MEIA exhibits solar cycle, seasonal, and local time variations. The occurrence rate of the MEIA is inversely dependent on solar activity. Occurrence of the MEIA maximizes near the equinoxes, with a primary (secondary) low occurrence rate near the June (December) solstice. In addition, occurrences of the MEIA are suppressed during the pre-reversal enhancement (PRE), resulting in relatively fewer events. Furthermore, it was found that the occurrence of the MEIA is not significantly dependent on the strength of geomagnetic activity. As far as we know, this study represents the first instance of utilizing observations from GOLD observations to investigate the characteristics of MEIA occurrences and their correlations with solar activity, season, and local time.

Keywords: nighttime merged EIA; occurrence characteristics of merged EIA; GOLD observation; airglow emission

Citation: Wu, K.; Qian, L. Occurrence Characteristics of Nighttime Merged EIA Based on NASA GOLD Observations from 2018 to 2023. *Remote Sens.* **2024**, *16*, 1575. https://doi.org/10.3390/rs16091575

Academic Editor: Angelo De Santis

Received: 26 March 2024
Revised: 23 April 2024
Accepted: 24 April 2024
Published: 29 April 2024

1. Introduction

The equatorial ionization anomaly (EIA) is usually characterized by two plasma density crests in the ionospheric F region, located near ± 15° off the magnetic equator [1,2]. The formation of EIA is typically attributed to the "fountain effect", resulting from vertical plasma drift and diffusion [1,3]. The occurrence and evolution characteristics of EIA have been extensively studied using observational data [4–11] and numerical models [12–15].

A unique feature of the EIA, known as merged EIA (MEIA), was reported by Carruthers and Page [16], followed by a small number of studies [15,17–21]. Using total electron content (TEC) data and Thermosphere Ionosphere Electrodynamics General Circulation Model (TIEGCM) simulations, Huang et al. [17] reported nighttime MEIA and suggested that the formation is related to the downward E × B effect during geomagnetic storm recovery phases. Balan et al. [18,19] employed Global Positioning System (GPS) TEC data to show MEIA during storm recovery phases. They further utilized the Sheffield University Plasmasphere Ionosphere Model and proposed that the formation of MEIA is related to equatorward storm-time neutral winds, downward E × B drifts, and an increase in the O/N_2 ratio. Huang et al. [20] used TEC data between 1999 and 2012 to study single-peak EIA at 120°E longitude and found that single-peak EIA predominantly occurs during low solar activity. Aa et al. [21] used observations from GOLD and Ionospheric Connection Explorer (ICON) to investigate the MEIA and attributed it to the impact of westward electric fields generated by zonal wind oscillations triggered by the eruption of the Tonga volcano on 15 January 2022. Wu et al. [15] reported an MEIA during a geomagnetic storm

on 4 November 2021 using observations from the GOLD mission. Based on the Whole Atmosphere Community Climate Model-eXtended (WACCM-X) simulations, they suggested that the formation of MEIA was attributed to the prolonged westward disturbance of dynamo electric fields (DDEF) during a geomagnetic storm.

It should be noted that the single-peak EIA encompasses various mechanisms, such as the formation of EIA through the merging of two EIA crests on 15 January 2022 and 27 August 2022 (see Supplementary Materials S1 and S4) or the formation of single-peak EIA due to the disappearance of another EIA crest (such as the EIA crests on 26 April 2023 and 27 August 2023; see Supplementary Materials S2 and S3). In previous studies [22,23], the instantaneous observations from in situ satellites on a single orbit are unable to identify the reasons for the formation of a single-peak EIA. These types have all been classified as single-peak EIA. The oxygen 135.6 nm emission observed by GOLD, on the other hand, represents the integral along the line of sight, which has the largest contribution from the F2 peak region (around 300 km), rather than just at a specific altitude. The time series of GOLD's 2D image provide the coverage of the longitude section where the merging of the northern and southern EIA crests occurs. This provides us with vital data for studying the occurrence MEIA and its correlation with solar activity, season, and local time, enabling us to investigate characteristics of MEIA occurrence that have not been studied before.

In this study, we utilized observations spanning over five years (October 2018 to the end of 2023) from the GOLD mission to conduct a statistical analysis of the occurrence characteristics of nighttime MEIA in the GOLD's field of view (FOV, ~70°W to 10°E). By statistically analyzing the 5-year observations (the dataset includes effective observations for 1454 days, with 283 days involving MEIA) from GOLD, we can gain a comprehensive understanding of the occurrence characteristics of nighttime MEIA. This significantly contributes to our understanding of the nighttime equatorial and low latitude ionosphere. Section 2 provides a description of the data and introduces analysis methods; Section 3 presents the statistical analysis results; Section 4 provides discussions of the results; Section 5 concludes the study.

2. Datasets and Statistical Analysis Methods

The datasets used in this study are from the NASA GOLD mission (https://gold.cs.ucf.edu/data/, accessed on 26 March 2024). The GOLD mission, equipped with a far-ultraviolet imager, captures Earth's airglow emission ranging from 134 nm to 162 nm. It operates with two distinct observation channels (A and B), with Channel A scanning the Northern Hemisphere and Channel B scanning the Southern Hemisphere. Nighttime observations mainly involve channel B (20:05–22:55 UT), and it alternately scans the Southern and Northern Hemispheres for 15 min each, providing a temporal resolution of 30 min. During the nighttime, GOLD captures oxygen 135.6 nm radiance with a spectral resolution of 0.4 nm and spatial resolution of $1^\circ \times 1^\circ$ [10,11,24]. The nighttime peak emission of oxygen 135.6 nm typically reflects the peak density of the ionosphere F2 region (Nmax). For the oxygen 135.6 nm radiance, GOLD measures the column-integrated emission rate along the line of sight [11,25–27]. In this study, we utilized these nighttime oxygen 135.6 nm emission data from the GOLD mission observations between 5 October 2018 and the end of 2023 (GOLD oxygen 135.6 nm emission data has been available online publicly since 5 October 2018: https://gold.cs.ucf.edu/data/, accessed on 26 March 2024).

There are primarily several types of GOLD nighttime images as shown in Figure 1. For the results in Figure 1a, it is evident that it is impossible to distinguish the presence of EIA. If this pattern persists throughout the entire day, we mark that day as an EIA unavailable day. The second category is the regular separated EIA (Figure 1b). If separated EIA crests are visible throughout the entire night, we classify it as a typical EIA day. For Figure 1c, it is evident that there is a clear merging of the north and south EIA crests in the form of an "X" (see Supplementary Material S1). For this type of EIA, regardless of when it occurs or at which longitude, we categorize that day as an MEIA day. It is important to note the three types of results in Figure 1, as given in panels (d)–(f). Type (d) EIA, although

showing only one peak at certain longitudes, becomes clear through the results in (d) and the evolution of the time series (see Supplementary Materials S2 and S3) that the occurrence of a single-peak EIA is due to the disappearance of another EIA crest. We categorize such days as non-MEIA. For the EIA in Figure 1e, although we find the process of two EIA crests merging into one (Figure 1e and Supplementary Material S4), we cannot ascertain whether the EIA crests are approaching each other or actually merging. Thus, in the merging region, we select a longitude at the merged region (such as −20° longitude in Figure 1e) and plot the corresponding latitudinal variation of oxygen 135.6 nm emission (Rayleigh) between latitudes 40°S and 40°N (Figure 1g), which show as a single-peak. In this case, days with such EIA are determined as MEIA days. For Figure 1f, it is not visually apparent whether EIA is present. We also employ the same method of selecting a longitude and plotting the corresponding oxygen 135.6 emission (Rayleigh), as shown in Figure 1h. The results in Figure 1 h do not confirm the presence of EIA, thus we categorize such days as EIA unavailable days. Therefore, based on the above definitions, we counted situations in Figure 1a,f, as EIA unavailable days, the days with no observation data from the GOLD mission, and the days when the GOLD mission has data available only for the Southern Hemisphere or the Northern Hemisphere were also counted as EIA unavailable days. There are 438 EIA unavailable days in total, which accounts for ~23% of the total days. Excluding unavailable days, the remaining days are considered effective observational days (1454 days). In addition, we categorize types (c) and (e) in Figure 1 as MEIA days.

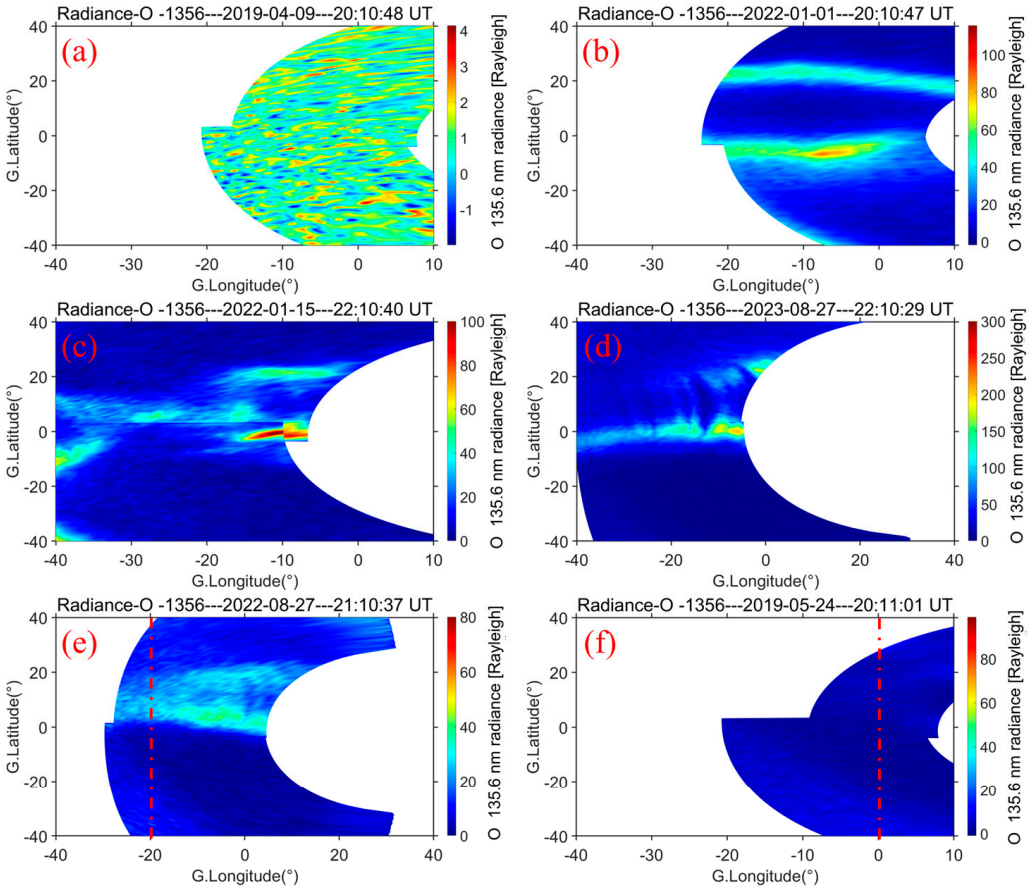

Figure 1. *Cont.*

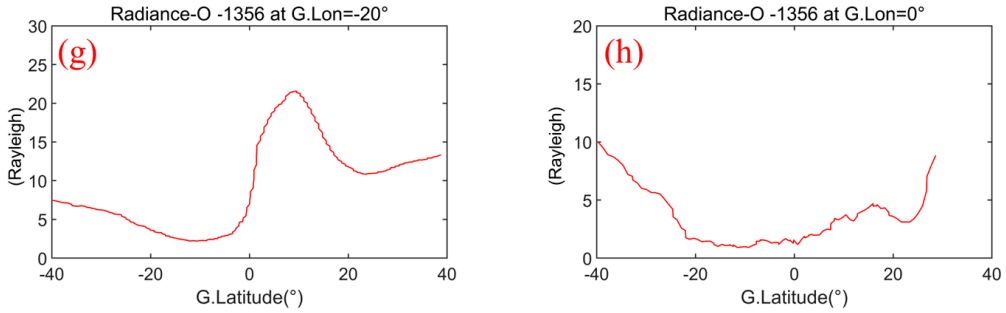

Figure 1. Observations from GOLD oxygen 135.6 nm emission. (**a**,**f**): EIA cannot be determined. (**b**,**d**): non-MEIA. (**c**,**e**): MEIA. (**g**,**h**): Latitudinal variations of the oxygen 135.6 Radiance (Rayleigh) at longitudes −20° and 0°, respectively (the red dashed lines). The G. Longitude and G. Latitude represent geographical longitude and geographical latitude.

3. Results

Figure 2 shows the statistical results of nighttime MEIA occurrences from October 2018 to the end of 2023. In Figure 2a, the green bars represent the number of effective observational days, the orange bars represent the days with MEIA, and the black bars represent the days with relatively strong geomagnetic activity during the MEIA days (a day is counted as a day with relatively strong geomagnetic activity if $|\mathrm{Dst}| > 30$ nT or $\sum \mathrm{Kp} \geq 16$). Each bar is labeled with the corresponding number of days. Figure 2a shows that between 2018 and 2023, the majority of MEIA occurrences were concentrated in the years 2019–2021, with no more than 100 days of occurrences per year. Starting from 2022, although the number of effective observation days was relatively high (>290 days), the occurrence days of MEIA suddenly began to decrease, with only 34 days and 5 days, which were fewer than in 2019 (50 days), 2020 (99 days), and 2021 (87 days). For a more accurate analysis of its occurrence rate, we present Figure 2b. In Figure 2b, the orange, black, and blue lines represent the occurrence rate of MEIA, the percentage of days with strong geomagnetic activity in the MEIA, and the yearly averaged F10.7 (F10.7 is solar radio flux at 10.7 cm, in unit of solar flux unit (sfu)), respectively (the orange and black lines correspond to values on the left *y*-axis). Figure 2 shows that MEIA had a relatively high occurrence rate (>20%) from October 2018 to 2021, with each year's occurrence rate exceeding 20%. However, starting from 2022, the occurrence rate sharply decreased, consistently falling below 10%, and notably, in 2023, it remained at only 2%. This occurrence rate has a clear correlation with the strength of solar activity. The yearly average F10.7 was less than 80 sfu from 2018 to 2021, indicating a period of low solar activity. Starting from 2022, the yearly average F10.7 exceeded 125 sfu, marking a period of higher solar activity. Therefore, the occurrence rate of nighttime MEIA exhibits an inverse correlation with the strength of solar activity. In addition, the black bars (black line) show that days (the percentage) with relatively strong geomagnetic activity during EIA occurrences vary across years, with some years exceeding 50% (2018, 2022, and 2023) and others falling below 50%. This suggests that the occurrence of nighttime MEIA does not show a significant correlation with the strength of geomagnetic activity.

To investigate seasonal dependence of the nighttime MEIA occurrence, we present monthly occurrence statistics of MEIA in each year in Figure 3. The green bars represent the effective observational days, the orange bars represent the days with MEIA (each non-zero bar is labeled with the corresponding number of days), and the red line represents the corresponding occurrence rates. Figure 3 shows varying monthly occurrence rates of MEIA, with most months showing rates below 50%. Only in certain months between 2019 and 2021 (primarily concentrated around April and September) does the rate exceed 50%. Figure 3 shows that MEIA occurrences exhibit distinct seasonal dependence. The peak occurrence is predominantly near the two equinoxes (months 2–4 and 8–10), with a primary low occurrence near the June solstice (months 5–7), and a secondary low occurrence near the December solstice (months 11, 12, and 1).

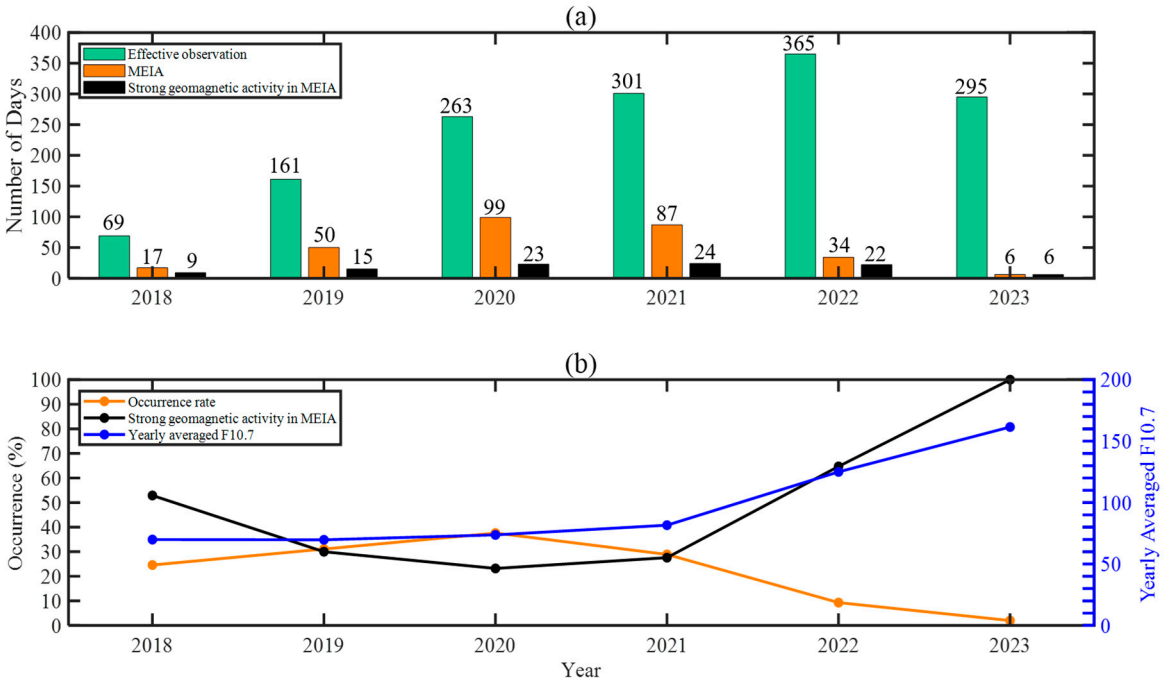

Figure 2. (**a**) The MEIA occurrence from 2018 to 2023. The green bars represent the number of effective observation days; the orange bars represent the number of days with MEIA occurrences. The black bars represent days with strong geomagnetic activity among the orange bar days. (**b**) The relationship between the occurrence rate of MEIA and solar activity. The orange, black, and blue lines represent occurrence rate of MEIA, the percentage of days with strong geomagnetic activity in the MEIA, and yearly average F10.7, respectively. The orange and black lines correspond to values on the left *y*-axis.

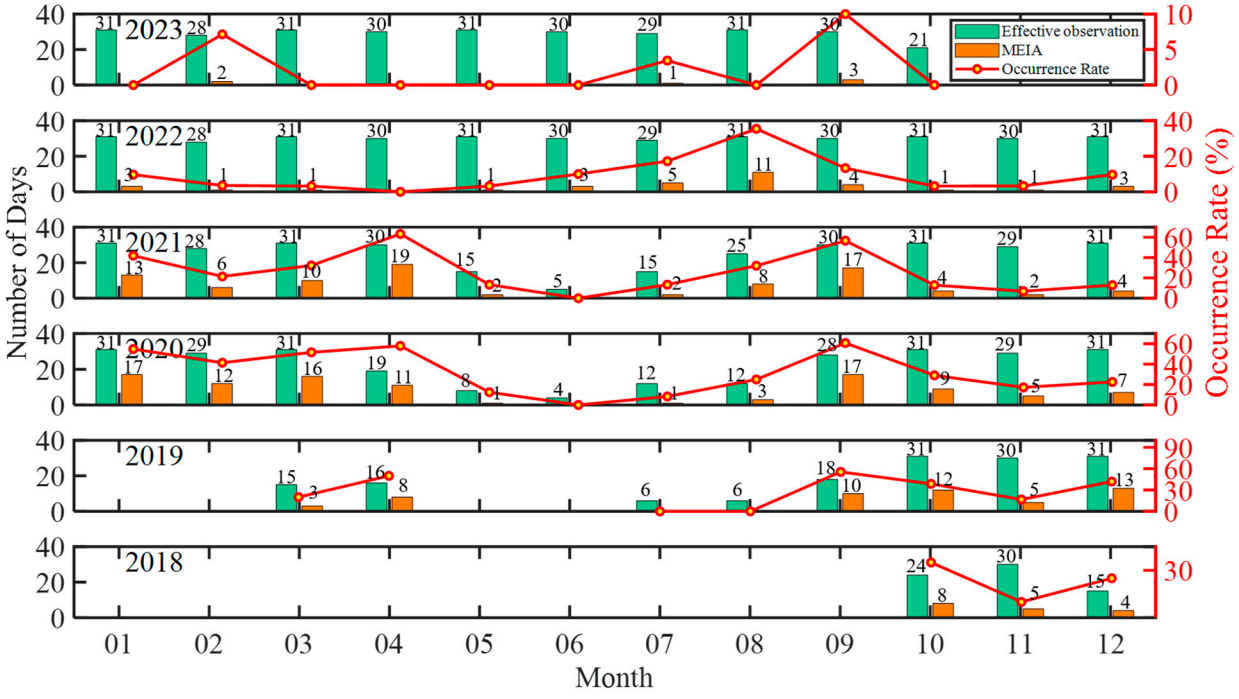

Figure 3. Statistics on the occurrence rate of merged EIA with respect to seasons. The green bars represent the number of effective observation days; the orange bars represent the number of days with merged EIA occurrence; the red line represents occurrence rate of the merged EIA.

In order to study the correlation between MEIA formation and local time, we conducted a statistical analysis of nighttime MEIA occurrences at longitudes 15°W (Figure 4a) and 30°W (Figure 4b) during three time intervals (19:00–20:00 local time (LT), 20:00–21:00 LT, 21:00–22:00 LT). The two longitudes were chosen since they are within the FOV of GOLD nighttime observations most of the time during the local time period of interest (~19:00 to ~22:00 LT). Each bar is labeled with the corresponding number of days. As shown in Figure 4, the occurrence days of MEIA are the lowest between 19:00 and 20:00 LT, followed by the occurrence days between 20:00 and 21:00 LT, and the highest occurrence days are between 21:00 and 22:00 LT. In addition, compared to longitude 15°W, the occurrence days of MEIA are higher at most time slots at longitude 30°W. Thus, Figure 4 shows two important characteristics of MEIA occurrences. Firstly, at longitudes 15°W and 30°W, occurrences before 20:00 LT are fewer than those after 20:00 LT. Secondly, the occurrence rate at 30°W is higher than the occurrence rate at 15°W. This indicates that the occurrence of nighttime MEIA exhibits both local time and longitude dependence.

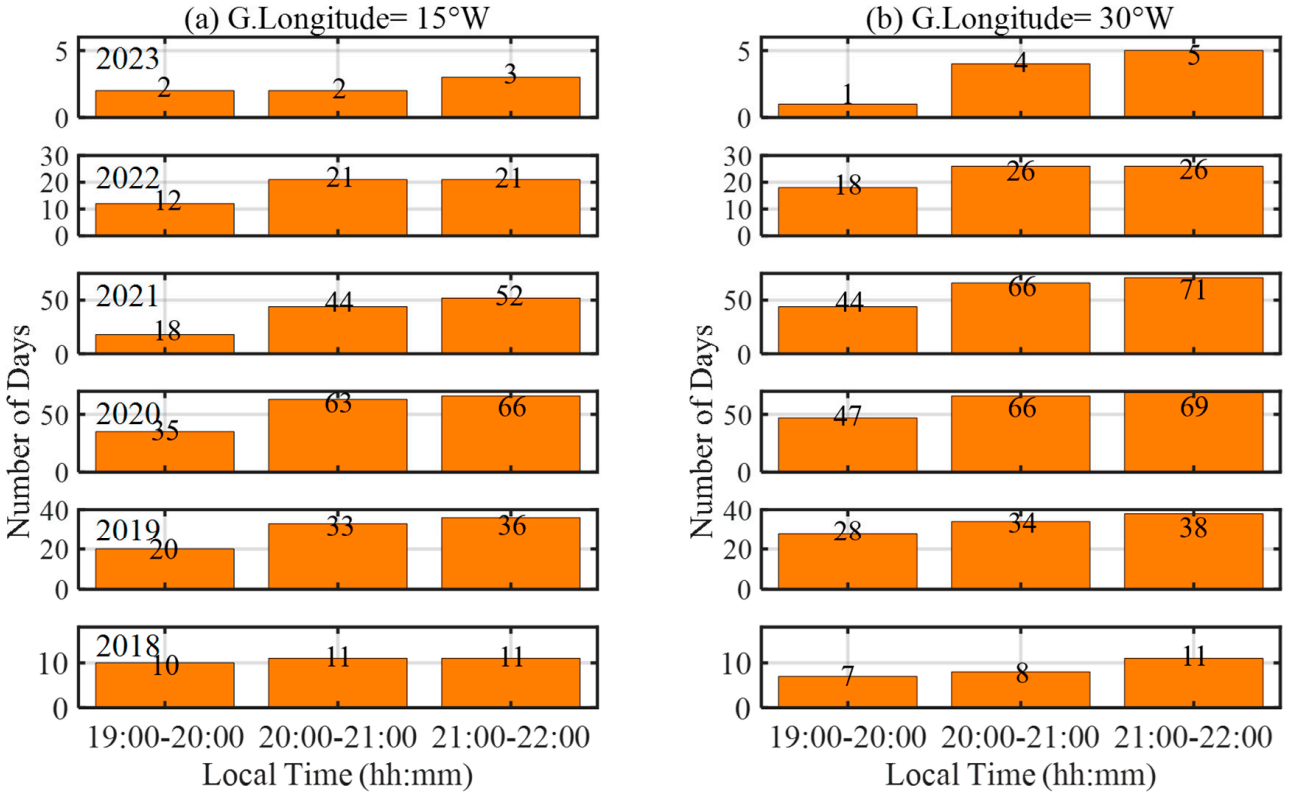

Figure 4. Statistics on the occurrence of the merged EIA at three time intervals (19:00–20:00, 20:00–21:00, and 21:00–22:00 LT) at longitudes 15°W (**a**) and 30°W (**b**), respectively.

4. Discussion

One of the statistical results is that the annual occurrence rate of MEIA shows a clear inverse relation with the strength of solar activity. The formation of this situation is partly attributed to the contraction of the whole ionosphere at low solar activity years. Some studies have shown that there is a noticeable decrease and contraction in ionospheric altitude during low solar activity years [28–30]. The contraction of the ionosphere leads to the approach of the crests of the north and south EIA, facilitating the formation of the MEIA. This is in contrast to high solar activity years. On the other hand, it is caused by differences in PRE upward plasma drifts during years of high and low solar activity. Previous studies found that, compared to low solar activity years, PRE upward plasma drifts were observed during high solar activity years [31–33]. Upward plasma drifts separate the EIA crests, which is unfavorable for the formation of nighttime MEIA. Solar activity in 2022 and 2023

(yearly averaged F10.7 > 125 sfu) is much higher than that in 2018–2021 (yearly averaged F10.7 < 80 sfu). Consequently, on average, the PRE vertical plasma drift velocity in the F region during 2022–2023 should be greater than that in 2018–2021, which is unfavorable for the formation of MEIA. This is likely attributed to the significant decline in the occurrence rate since 2022. However, it should be noted that the years covered in this study primarily include the solar minimum period between the 24th and 25th solar cycles, as well as the ascending phase of the 25th solar cycle. Compared to the majority of previous solar cycles, this period has relatively weak solar activity. It remains uncertain whether there will be differences in results during solar maximum when solar activity is stronger than during this period. More studies will be necessary in the future.

Another important occurrence characteristic of nighttime MEIA is its seasonal variation. At equinoxes, the occurrence of MEIA often reaches its maximum, followed by the Northern Hemisphere winter and then the Northern Hemisphere summer. The most likely cause of this seasonal variation is the modulation by neutral winds [34–36]. At nighttime, meridional winds tend to be equatorward due to high latitude Joule heating, which is a favorable condition for the formation of the MEIA. In the solstice seasons, there is a prevailing summer-to-winter large-scale circulation. This seasonal meridional circulation could hinder the formation of the MEIA depending on its strength. Furthermore, the seasonal variations in vertical plasma drift in the equatorial region should also be considered as an important factor contributing to the seasonal variations in MEIA. Some previous studies have already shown that, during years of solar minimum activity, the average downward vertical plasma drift after sunset is greater at the equinox than in summer [37]. This will also favor the formation of MEIA near the equinoxes. Another interesting phenomenon is the difference in the occurrence rates between the two solstice seasons. The occurrence rate near the June solstice is significantly lower than the occurrence rate near the December solstice season. This is likely related to the ionosphere annual asymmetry [38,39], which is the phenomenon of the ionosphere electron density being higher near the December solstice season than near the June solstice season. Figure 3 shows that the ionosphere annual asymmetry (green bars) is more prominent during lower solar activity years (2019, 2020, 2021).

In addition to the above two occurrence characteristics, the variations in local time and longitude of the nighttime MEIA occurrences are also important characteristics worth discussing. For the variation in the occurrence rate of MEIA with local time, it should be closely related to the post-sunset PRE. After sunset, there is almost daily occurrence of PRE [40–42], causing an enhancement of the eastward electric field in the equatorial region. The intensified eastward electric field, through E × B forcing, leads to an upward plasma drift, separating the EIA crests, and thus, is unfavorable for the formation of MEIA. Compared to after 20:00 LT, the period before 20:00 LT is closer to sunset, and the influence of PRE is stronger. Therefore, before 20:00 LT, the occurrence of MEIA is relatively lower. After 20:00 LT, the wind-driven polarization electric field becomes westward, causing the ionospheric plasma to move downward, which is conducive to the formation of MEIA. As the GOLD satellite cannot continuously observe a large range of longitudes over consecutive time intervals, for the longitude characteristics, we can only deduce that the occurrence rates of MEIA vary with longitude. Note these results are based on GOLD observations which cover the American and Atlantic Ocean longitudes (~70°W to 10°E). Occurrence statistics can be different in different longitude regions. A more in-depth analysis of the longitude distribution of occurrence rates should be investigated in the future with the assistance of additional observational data.

As for the impact of geomagnetic activity, previous studies have found that during geomagnetic storms, the disturbance electric field induced by the storms may enhance the PRE [43–45], leading to an increased upward drift of the plasma. Alternatively, it is possible for a westward DDEF formed during the storm to suppress the PRE [15,46–49], causing the plasma to drift downward. Thus, geomagnetic activity may either promote or suppress the generation of nighttime MEIA.

Previous studies investigating the occurrence characteristics of single-peak EIA were mainly based on statistical analysis of in situ satellite observations [22,23]. For observations made by in situ low earth orbiting (LEO) satellites, the altitude where the EIA crests merge to one is very important since the observations are made at altitudes of the satellite orbits. In other words, the Swarm satellites observe the EIA at ~460 km altitudes (Swarm A and C) and ~530 km altitudes (Swarm B). The oxygen 135.6 nm emission (Rayleigh) observed by GOLD represents the integral along the line of sight, which has the largest contribution from the F2 peak region, rather than just the results at a specific altitude. The time series of GOLD's 2D image provides realistic views/data of the longitudes where the merging of the northern and southern EIA crests occurs. In addition, the statistics from these previous studies [22,23] largely represent daytime events since a majority of the events in these studies occurred during daytime (~85% occurred between 08:00–12:00 UT), whereas our events are entirely nighttime events. The photochemistry, dynamics, and electrodynamics of daytime and nighttime ionosphere are significantly different. Thus, our statistical study not only provides detailed insight into the occurrence characteristics of nighttime MEIA but also fills a crucial gap in the studies of single-peak EIA observed by in situ satellites [17,20,22,23].

5. Conclusions

In this study, we utilized over five years of observational data from the GOLD mission, from October 2018 to the end of 2023, to investigate the occurrence characteristics of nighttime MEIA in the GOLD's FOV (~70°W to 10°E). To our knowledge, this study represents the first set of statistical analyses of the relationship between the occurrence characteristics of MEIA and solar activity, season, and local time using a time series of 2D observations from the GOLD mission. The occurrence of the MEIA shows dependence on solar activity, season, and local time. The occurrence rate of the MEIA has a correlation with the strength of solar activity, with the occurrence rate of the MEIA being inversely dependent on solar activity strength. The occurrence rate of the MEIA maximizes near the equinoxes (months 2–4 and 8–10), with a primary minimum near the June solstice (months 5–7) and a secondary minimum near the December solstice (months 11, 12, and 1). This annual asymmetry of MEIA occurrence rates is consistent with the ionospheric annul asymmetry of electron density. They are likely related. In addition, occurrences of the MEIA are suppressed near the PRE, resulting in relatively fewer events. The occurrence of MEIA exhibits both local time and longitude dependence. Furthermore, there is no significant correlation between the occurrence rate of the MEIA and the strength of geomagnetic activity.

Supplementary Materials: The following supporting information can be downloaded at: https://www.mdpi.com/article/10.3390/rs16091575/s1. The supplementary materials provide four movies: Movies S1–S4. Movie S1: The detailed evolution process of the oxygen 135.6 Radiance (Rayleigh) observed by GOLD during the night of 15 January 2022. The evolution involves the formation of an "X"-shaped MEIA. Movie S2: The detailed evolution process of the oxygen 135.6 Radiance (Rayleigh) observed by GOLD during the night of 26 April 2023. The single-peak EIA crest observed at certain longitudes is due to the disappearance of the Northern Hemisphere EIA crest and it is not MEIA. Movie S3: The detailed evolution process of the oxygen 135.6 Radiance (Rayleigh) observed by GOLD during the night of 27 August 2023. Similar to Movie S2, the single-peak EIA crest observed at certain longitudes is due to the disappearance of the Northern Hemisphere EIA crest and it is not MEIA. Movie S4: The detailed evolution process of the oxygen 135.6 Radiance (Rayleigh) observed by GOLD during the night of 27 August 2022. It can be clearly seen that two EIA crests merge into one.

Author Contributions: Conceptualization, K.W. and L.Q.; methodology, K.W. and L.Q.; formal analysis, K.W. and L.Q.; investigation, K.W. and L.Q.; resources, K.W.; data curation, K.W.; writing-original draft preparation, K.W.; writing—review and editing, K.W. and L.Q.; visualization, all authors; supervision, all authors; project administration, L.Q.; funding acquisition, L.Q. All authors have read and agreed to the published version of the manuscript.

Funding: This study is supported by NASA grants 80NSSC20K0189, 80NSSC19K0278, 80NSSC19K0835, 80NSSC19K0356, 80NSSC20K1350, and NNH19ZDA001N-HTMS. This work is also supported in part by the NASA contract 80GSFC18C0061 to the University of Colorado and by the NASA DRIVE Science Center for Geospace Storms (CGS) under award 80NSSC22M0163. The National Center for Atmospheric Research is a major facility sponsored by the National Science Foundation under Cooperative Agreement No. 1852977.

Data Availability Statement: The GOLD data used in the study can be downloaded at https://gold.cs.ucf.edu/data/search/, accessed on 26 March 2024. The Dst, Kp, and F10.7 data are obtained from the OMNIWeb service https://cdaweb.gsfc.nasa.gov/, accessed on 26 March 2024.

Acknowledgments: We acknowledge the GOLD team and the OMNIWeb service (https://cdaweb.gsfc.nasa.gov/, accessed on 26 March 2024) for providing the data used in the study. We acknowledge the support of this study by NASA and NSF funding.

Conflicts of Interest: The authors declare no conflicts of interest.

References

1. Appleton, E.V. Two anomalies in the ionosphere. *Nature* **1946**, *157*, 691. [CrossRef]
2. Croom, S.; Robbins, A.; Thomas, J.O. Two anomalies in the behaviour of the F2 layer of the ionosphere. *Nature* **1959**, *184*, 2003–2004. [CrossRef]
3. Duncan, R.A. The equatorial f-region of the ionosphere. *J. Atmos. Terr. Phys.* **1960**, *18*, 89–100. [CrossRef]
4. Anderson, D.N. A theoretical study of the ionospheric F region equatorial anomaly—I. Theory. *Planet. Space Sci.* **1973**, *21*, 409–419. [CrossRef]
5. Balan, N.; Liu, L.; Le, H. A brief review of equatorial ionization anomaly and ionospheric irregularities. *Earth Planet. Phys.* **2018**, *2*, 257–275. [CrossRef]
6. Balan, N.; Bailey, G.J.; Abdu, M.A.; Oyama, K.I.; Richards, P.G.; MacDougall, J.; Batista, I.S. Equatorial plasma fountain and its effects over three locations: Evidence for an additional layer, the F 3 layer. *J. Geophys. Res. Space Phys.* **1997**, *102*, 2047–2056. [CrossRef]
7. Basu, S.; Huba, J.; Krall, J.; McDonald, S.E.; Makela, J.J.; Miller, E.S.; Ray, S.; Groves, K. Day-to-day variability of the equatorial ionization anomaly and scintillations at dusk observed by guvi and modeling by sami3. *J. Geophys. Res. Space Phys.* **2009**, *114*, A04302. [CrossRef]
8. Zhang, M.-L.; Wan, W.; Liu, L.; Ning, B. Variability study of the crest-to-trough TEC ratio of the equatorial ionization anomaly around 120°E longitude. *Adv. Space Res.* **2009**, *43*, 1762–1769. [CrossRef]
9. Khadka, S.M.; Valladares, C.E.; Sheehan, R.; Gerrard, A.J. Effects of electric field and neutral wind on the asymmetry of equatorial ionization anomaly. *Radio Sci.* **2018**, *53*, 683–697. [CrossRef]
10. Cai, X.; Burns, A.G.; Wang, W.; Qian, L.; Liu, J.; Solomon, S.C.; Eastes, R.W.; Daniell, R.E.; Martinis, C.R.; McClintock, W.E.; et al. Observation of postsunset OI 135.6 nm radiance enhancement over South America by the GOLD mission. *J. Geophys. Res. Space Phys.* **2021**, *126*, e28108. [CrossRef]
11. Cai, X.; Burns, A.G.; Wang, W.; Coster, A.; Qian, L.; Liu, J.; Solomon, S.C.; Eastes, R.W.; Daniell, R.E.; McClintock, W.E. Comparison of GOLD nighttime measurements with total electron content: Preliminary results. *J. Geophys. Res. Space Phys.* **2020**, *125*, e27767. [CrossRef]
12. Zeng, Z.; Burns, A.; Wang, W.; Lei, J.; Solomon, S.; Syndergaard, S.; Qian, L.; Kuo, Y.-H. Ionospheric annual asymmetry observed by the COS-MIC radio occultation measurements and simulated by the TIEGCM. *J. Geophys. Res.* **2008**, *113*, A07305. [CrossRef]
13. Dang, T.; Luan, X.; Lei, J.; Dou, X.; Wan, W. A numerical study of the interhemispheric asymmetry of the equatorial ionization anomaly in solstice at solar minimum. *J. Geophys. Res. Space Phys.* **2016**, *121*, 9099–9110. [CrossRef]
14. Cai, X.; Qian, L.; Wang, W.; McInerney, J.M.; Liu, H.; Eastes, R.W. Investigation of the post-sunset extra electron density peak poleward of the equatorial ionization anomaly southern crest. *J. Geophys. Res. Space Phys.* **2022**, *127*, e2022JA030755. [CrossRef]
15. Wu, K.; Qian, L.; Wang, W.; Cai, X.; Mclnerney, J.M. Investigation of the GOLD observed merged nighttime EIA with WACCM-X simulations during the storm of 3 and 4 November 2021. *Geophys. Res. Lett.* **2023**, *50*, e2023GL103603. [CrossRef]
16. Carruthers, G.R.; Page, T. Apollo 16 far-ultraviolet camera/spectrograph: Earth observations. *Science* **1972**, *177*, 788–791. [CrossRef] [PubMed]
17. Huang, C.M.; Chen, M.Q.; Liu, J.Y. Ionospheric positive storm phases at the magnetic equator close to sunset. *J. Geophys. Res.* **2010**, *115*, A07315. [CrossRef]
18. Balan, N.; Yamamoto, M.; Liu, J.Y.; Otsuka, Y.; Liu, H.; Lühr, H. New aspects of thermospheric and ionospheric storms revealed by CHAMP. *J. Geophys. Res. Space Phys.* **2011**, *116*, A07305. [CrossRef]
19. Balan, N.; Otsuka, Y.; Nishioka, M.; Liu, J.Y.; Bailey, G.J. Physical mechanisms of the ionospheric storms at equatorial and higher latitudes during the recovery phase of geomagnetic storms. *J. Geophys. Res. Space Phys.* **2013**, *118*, 2660–2669. [CrossRef]

20. Huang, L.; Wang, J.; Jiang, Y.; Huang, J.; Chen, Z.; Zhao, K. A preliminary study of the single crest phenomenon in total electron content (TEC) in the equatorial anomaly region around 120 E longitude between 1999 and 2012. *Adv. Space Res.* **2014**, *54*, 2200–2207. [CrossRef]
21. Aa, E.; Zhang, S.; Wang, W.; Erickson, P.J.; Qian, L.; Eastes, R.; Harding, B.J.; Immel, T.J.; Karan, D.K.; Daniell, R.E.; et al. Pronounced suppression and X-pattern merging of equatorial ionization anomalies after the 2022 Tonga volcano eruption. *J. Geophys. Res. Space Phys.* **2022**, *127*, e2022JA030527. [CrossRef] [PubMed]
22. Fathy, A.; Ghamry, E. A statistical study of single crest phenomenon in the equatorial ionospheric anomaly region using Swarm A satellite. *Adv. Space Res.* **2017**, *59*, 1539–1547. [CrossRef]
23. Hussien, F.; Ghamry, E.; Mohammed, Y.; Fathy, A. Ionospheric single crest events at different altitudes and activity levels observed by Swarm constellation. *Astrophys. Space Sci.* **2023**, *368*, 25. [CrossRef]
24. Eastes, R.W.; Solomon, S.C.; Daniell, R.E.; Anderson, D.N.; Burns, A.G.; England, S.L.; Martinis, C.R.; McClintock, W.E. Global-scale observations of the equatorial ionization anomaly. *Geophys. Res. Lett.* **2019**, *46*, 9318–9326. [CrossRef]
25. Eastes, R.W.; McClintock, W.E.; Burns, A.G.; Anderson, D.N.; Andersson, L.; Codrescu, M.; Correira, J.T.; Daniell, R.E.; England, S.L.; Evans, J.S.; et al. The global-scale observations of the limb and disk (GOLD) mission. *Space Sci. Rev.* **2017**, *212*, 383–408. [CrossRef]
26. Karan, D.K.; Daniell, R.E.; England, S.L.; Martinis, C.R.; Eastes, R.W.; Burns, A.G.; McClintock, W.E. First zonal drift velocity measurement of equatorial plasma bubbles (EPBs) from a geostationary orbit using GOLD data. *J. Geophys. Res. Space Phys.* **2020**, *125*, e2020JA028173. [CrossRef]
27. McClintock, W.E.; Eastes, R.W.; Hoskins, A.C.; Siegmund, O.H.W.; McPhate, J.B.; Krywonos, A.; Solomon, S.C.; Burns, A.G. Global-scale observations of the limb and disk mission implementation: 2. Observations, data pipeline, and level 1 data products. *J. Geophys. Res. Space Phys.* **2020**, *125*, e2020JA027809. [CrossRef]
28. Heelis, R.A.; Coley, W.R.; Burrell, A.G.; Hairston, M.R.; Earle, G.D.; Perdue, M.D.; Power, R.A.; Harmon, L.L.; Holt, B.J.; Lippincott, C.R. Behavior of the O^+/H^+ transition height during the extreme solar minimum of 2008. *Geophys. Res. Lett.* **2009**, *36*, L00C03. [CrossRef]
29. Liu, L.; Chen, Y.; Le, H.; Kurkin, V.I.; Polekh, N.M.; Lee, C.-C. The ionosphere under extremely prolonged low solar activity. *J. Geophys. Res. Space Phys.* **2011**, *116*, A04320. [CrossRef]
30. Nanan, B.; Chen, C.Y.; Rajesh, P.K.; Liu, J.Y.; Bailey, G.J. Modeling and observations of the low latitude ionosphere-plasmasphere system at long deep solar minimum. *J. Geophys. Res. Space Phys.* **2012**, *117*, A08316. [CrossRef]
31. Fejer, B.G.; Farley, D.T.; Woodman, R.; Calderon, C. Dependence of equatorial F region vertical drifts on season and solar cycle. *J. Geophys. Res. Space Phys.* **1979**, *84*, 5792–5796. [CrossRef]
32. Batista, I.S.; de Medeiros, R.T.; Abdu, M.A.; de Souza, J.R.; Bailey, G.J.; de Paula, E.R. Equatorial ionospheric vertical plasma drift model over the Brazilian region. *J. Geophys. Res. Space Phys.* **1996**, *101*, 10887–10892. [CrossRef]
33. Abdu, M.A.; Batista, I.S.; Reinisch, B.W.; Sobral, J.H.A.; Carrasco, A.J. Equatorial F region evening vertical drift, and peak height, during southern winter months: A comparison of observational data with the IRI descriptions. *Adv. Space Res.* **2006**, *37*, 1007–1017. [CrossRef]
34. Liu, J.; Zhang, D.; Mo, X.; Xiong, C.; Hao, Y.; Xiao, Z. Morphological differences of the northern equatorial ionization anomaly between the eastern Asian and American sectors. *J. of Geophys. Res.* **2020**, *125*, e2019JA027506. [CrossRef]
35. Tsai, H.; Liu, J.; Tsai, W.; Liu, C.; Tseng, C.; Wu, C. Seasonal variations of the ionospheric total electron content in Asian equatorial anomaly regions. *J. Geophys. Res.* **2001**, *106*, 30363–30369. [CrossRef]
36. Huang, Y.; Cheng, K. Solar cycle variations of the equatorial ionospheric anomaly in total electron content in the Asian region. *J. Geophys. Res.* **1996**, *101*, 24513–24520. [CrossRef]
37. Fejer, B.G.; de Paula, E.R.; Heelis, R.A.; Hanson, W.B. Global equatorial ionospheric vertical plasma drifts measured by the AE-E satellite. *J. Geophys. Res. Space Phys.* **1996**, *100*, 5769–5776. [CrossRef]
38. Burns, A.G.; Solomon, S.C.; Wang, W.; Qian, L.; Zhang, Y.; Paxton, L.J. Daytime climatology of ionospheric NmF2 and hmF2 from COSMIC data. *J. Geophys. Res.* **2012**, *117*, A09315. [CrossRef]
39. Qian, L.; Burns, A.G.; Solomon, S.C.; Wang, W. Annual/semiannual variation of the ionosphere. *Geophys. Res. Lett.* **2013**, *40*, 1928–1933. [CrossRef]
40. Farley, D.T.; Bonelli, E.; Fejer, B.G.; Larsen, M.F. The prereversal enhancement of the zonal electric field in the equatorial ionosphere. *J. Geophys. Res. Atmos.* **1986**, *91*, 13723–13728. [CrossRef]
41. Millward, G.H.; Müller-Wodarg, I.C.F.; Aylward, A.D.; Fuller-Rowell, T.J.; Richmond, A.D.; Moffett, R.J. An investigation into the influence of tidal forcing on f region equatorial vertical ion drift using a global ionosphere-thermosphere model with coupled electrodynamics. *J. Geophys. Res. Space Phys.* **2001**, *106*, 24733–24744. [CrossRef]
42. Mathew, T.J.; Nayar, S. Vertical shear at the equatorial f-region ionosphere during post-sunset hours. *Adv. Space Res.* **2012**, *49*, 1277–1281. [CrossRef]
43. Abdu, M.A.; Batista, I.S.; Takahashi, H.; MacDougall, J.; Sobral, J.H.; Medeiros, A.F.; Trivedi, N.B. Magnetospheric disturbance Induced equatorial plasma bubble development and dynamics: A case study in Brazilian sector. *J. Geophys. Res.* **2003**, *108*, 1449. [CrossRef]

44. Basu, S.; Basu, S.; Rich, F.J.; Groves, K.M.; MacKenzie, E.; Coker, C.; Sahai, Y.; Fagundes, P.R.; Becker-Guedes, F. Response of the equatorial ionosphere at dusk to penetration electric fields during intense magnetic storms. *J. Geophys. Res.* **2007**, *112*, A08308. [CrossRef]
45. Tulasi Ram, S.; Rama Rao, P.V.S.; Prasad, D.S.V.V.D.; Niranjan, K.; Gopi Krishna, S.; Sridharan, R.; Ravindran, S. Local time dependent response of postsunset ESF during geomagnetic storms. *J. Geophys. Res.* **2008**, *113*, A07310. [CrossRef]
46. Scherliess, L.; Fejer, B.G. Storm time dependence of equatorial disturbance dynamo zonal electric fields. *J. Geophys. Res.* **1997**, *102*, 24037–24046. [CrossRef]
47. Li, G.; Ning, B.; Zhao, B.; Liu, L.; Wan, W.; Ding, F.; Xu, J.S.; Liu, J.Y.; Yumoto, K. Characterizing the 10 November 2004 storm-time middle-latitude plasma bubble event in Southeast Asia using multi-instrument observations. *J. Geophys. Res.* **2009**, *114*, A07304. [CrossRef]
48. Ramsingh; Sripathi, S.; Sreekumar, S.; Banola, S.; Emperumal, K.; Tiwari, P.; Kumar, B.S. Low-latitude ionosphere response to super geomagnetic storm of 17/18 March 2015: Results from a chain of ground-based observations over Indian sector. *J. Geophys. Res. Space Phys.* **2015**, *120*, 10864–10882. [CrossRef]
49. Carter, B.A.; Yizengaw, E.; Pradipta, R.; Retterer, J.M.; Groves, K.; Valladares, C.; Caton, R.; Bridgwood, C.; Norman, R.; Zhang, K. Global equatorial plasma bubble occurrence during the 2015 St. Patrick's Day storm. *J. Geophys. Res. Space Phys.* **2016**, *121*, 894–905. [CrossRef]